ERCOFTAC Bullentin No. 40: March 1999, pp. 51-58 (Eq. 8 has been corrected)

LARGE EDDY SIMULATION FOR FLUID FLOW AND HEAT TRANSFER

Lars Davidson
Dept. of Thermo and Fluid Dynamics, Chalmers University of Technology
SE-412 96 Gothenburg, Sweden, http://www.tfd.chalmers.se/~lada

Introduction

The present paper gives a review of the activities of the author's group on Large Eddy Simulation. Standard finite volume methods are employed which are second-order accurate in space and time. In "Numerical Method I" (see below), the pressure-velocity coupling is treated with a two-step time advancement method. Unlike most methods in the literature, our method is *implicit*. This gives us a certain freedom concerning the time steps, as we have no numerical requirement to maintain the CFL number below one. Of course, the time step should still be of the order of $CFL \simeq 1$, to keep numerical accuracy. However, we believe that in many situations we can locally admit $CFL \simeq 2$.

The "Numerical Method II" is a multiblock code which is parallelized using PVM. This parallelization is suitable on both shared-memory and distributed-memory machines. The pressure-velocity coupling is in this solver handled by SIMPLEC or PISO.

Most of our work on subgrid modelling is directed towards complex geometries. This means that we do not rely on the requirement of any homogeneous assumption. In the standard Germano model, the dynamic coefficient fluctuates "wildly" in both space and time, and it destroys the stability of numerical algorithms. To stabilize the numerical algorithm, the dynamic coefficient is commonly averaged in some direction or is clipped in an *ad hoc* manner. The present author has developed a dynamic one-equation model in which there is no need to spanwise average and/or to clip the dynamic coefficients at all. The reason is that the local dynamic coefficients appear only in source terms of the transport equation for the kinetic subgrid energy, k_{sgs}. In this way, the strong oscillations in the dynamic coefficients are smoothed out in a natural way by convection and diffusion. Another advantage of the dynamic one-equation model is that it can handle negative values of the dynamic coefficient, C, which appears in the production terms of the k_{sgs} equation. A negative C implies negative production (backscatter), which reduces k_{sgs} (and also the turbulent, subgrid viscosity since $\nu_{sgs} \propto k_{sgs}^{\frac{1}{2}}$, see below). Note that the magnitude of negative ν_{sgs} is not limited in any way.

Below are presented the two numerical methods, followed by a description of the dynamic one-equation subgrid model. After that a relatively large section of results is presented.

Numerical Method I

This numerical method is an implicit, two-step time-advancement method. The filtered Navier-Stokes equation for the $\bar{u}_i$ velocity reads

$$\frac{\partial \bar{u}_i}{\partial t} + \frac{\partial}{\partial x_j}\left(\bar{u}_i \bar{u}_j\right) = -\frac{1}{\rho}\frac{\partial \bar{p}}{\partial x_i} + \nu \frac{\partial^2 \bar{u}_i}{\partial x_j \partial x_j} - \frac{\partial \tau_{ij}}{\partial x_j}. \quad (1)$$

When discretized, it can be written

$$\begin{aligned} \bar{u}_i^{n+1} &= \bar{u}_i^n + \Delta t H\left(\bar{u}_i^n, \bar{u}_i^{n+1}\right) - \frac{1}{\rho}\alpha \Delta t \frac{\partial \bar{p}^{n+1}}{\partial x_i} \\ &- \frac{1}{\rho}(1-\alpha)\Delta t \frac{\partial \bar{p}^n}{\partial x_i} \end{aligned} \quad (2)$$

where $H\left(\bar{u}_i^n, \bar{u}_i^{n+1}\right)$ includes convection and the viscous and subgrid stresses and $\alpha = 0.5$ (Crank-Nicolson). Central differencing in space is used for all terms, which makes the discretization second-order accurate in space and time. Equation 2 is solved – employing a symmetric point-by-point Gauss-Seidel solver – which gives $\bar{u}_i^{n+1}$, which does not satisfy continuity. An intermediate velocity field is computed by subtracting the implicit part of the pressure gradient, i.e.

$$\bar{u}_i^* = \bar{u}_i^{n+1} + \frac{1}{\rho}\alpha \Delta t \frac{\partial \bar{p}^{n+1}}{\partial x_i}. \quad (3)$$

Taking the divergence of Eq. 3 requiring that continuity (for the face velocities $\bar{u}_{i,f}^*$, which are obtained by linear interpolation) should be satisfied on level $n+1$, i.e. $\partial \bar{u}_{i,f}^{n+1}/\partial x_i = 0$, we obtain

$$\frac{\partial^2 \bar{p}^{n+1}}{\partial x_i \partial x_i} = \frac{\rho}{\Delta t \alpha}\frac{\partial \bar{u}_{i,f}^*}{\partial x_i}. \quad (4)$$

This Poisson equation is solved employing an efficient, nested multigrid solver [8]. For more detail on the numerical method, see Refs. [5, 8, 29].

The code was parallelized by Zacharov [36]. The parallelization is made on the loop level using compiler directives, which means that the parallelization is suitable only on shared-memory machines. On a 1.3 million node mesh, a speed-up of 6.3 was achieved on eight processors on Chalmers' 64-processor CRAY 2000 Origin machine.

This code has been used in all calculations presented below, except in the LESFOIL project.

Numerical Method II

This numerical method was originally based on the standard SIMPLEC procedure. The computational domain is generated as a multiblock grid. The equations are solved in each block, in parallel, and the inner boundary conditions, stemming from the domain decomposition, are exchanged using message passing (PVM). For more details, see Ref. [23].

This code was later extended to LES (central differencing for discretization of the the convection terms and Crank-Nicolson for time discretization), and the PISO algorithm was implemented [1]. The finite volume discretization of the method is identical to that for "Numerical Method I", except for the Rhie-Chow interpolation

In the LESFOIL project (see below), this code was used on Chalmers' 64-processor Sun Enterprise, and super-linear performance has been achieved on

up to 32 processors using PISO [2]. Two iterations were required each time step to reach convergence ($CFL_{max} \simeq 1$).

The Dynamic One-Equation Subgrid Model

A new dynamic one-equation subgrid model has recently been presented [3]. For convenience, the model is briefly described below.

The modelled k_{sgs} equation can be written

$$\begin{aligned}
\frac{\partial k_{sgs}}{\partial t} + \frac{\partial}{\partial x_j}(\bar{u}_j k_{sgs}) &= \frac{\partial}{\partial x_j}\left(\langle C\rangle_{xyz}\Delta k_{sgs}^{\frac{1}{2}}\frac{\partial k_{sgs}}{\partial x_j}\right) \\
&+ P_{k_{sgs}} - C_*\frac{k_{sgs}^{\frac{3}{2}}}{\Delta} \\
P_{k_{sgs}} = -\tau_{ij}^a \bar{u}_{i,j}, \quad \bar{S}_{ij} &= \frac{1}{2}\left(\frac{\partial \bar{u}_i}{\partial x_j} + \frac{\partial \bar{u}_j}{\partial x_i}\right) \\
\tau_{ij}^a = -2C\Delta k_{sgs}^{\frac{1}{2}}\bar{S}_{ij} &= -2\nu_{sgs}\bar{S}_{ij}. \qquad (5)
\end{aligned}$$

In the production term, the dynamic coefficient, C, is computed in a way similar to that used in the standard dynamic model [10–13], i.e.

$$\begin{aligned}
C &= -\frac{\mathcal{L}_{ij}M_{ij}}{2M_{ij}M_{ij}}, \quad \mathcal{L}_{ij} = \widehat{\bar{u}_i\bar{u}_j} - \widehat{\bar{u}}_i\widehat{\bar{u}}_j \qquad (6) \\
K &= \widehat{k}_{sgs} + \frac{1}{2}\mathcal{L}_{ii}, \quad M_{ij} = \widehat{\Delta}K^{\frac{1}{2}}\widehat{\bar{S}}_{ij} - \Delta\,\widehat{k_{sgs}^{\frac{1}{2}}\bar{S}_{ij}}
\end{aligned}$$

where $\mathcal{L}_{ij}$ denotes the *dynamic* Leonard stresses, and where $K \equiv \frac{1}{2}T_{ii}$ is the subgrid kinetic energy on the test level [4, 12, 13].

To ensure numerical stability, a *constant* value of C in space ($\langle C\rangle_{xyz}$) is used in the momentum equations. This is determined by requiring that the production in the whole computational domain remains the same, i.e.

$$\langle 2C\Delta k_{sgs}^{\frac{1}{2}}\bar{S}_{ij}\bar{S}_{ij}\rangle_{xyz} = 2\langle C\rangle_{xyz}\langle \Delta k_{sgs}^{\frac{1}{2}}\bar{S}_{ij}\bar{S}_{ij}\rangle_{xyz}. \qquad (7)$$

The dynamic coefficient in front of the dissipation term in Eq. 5 remains to be determined. Subgrid scales on grid and test filter are close to being in local equilibrium. We assume that the convective and diffusive transport of k_{sgs} and K are equal, which gives [3]

$$C_*^{n+1} = \left(P_K - \widehat{P}_{k_{sgs}} + \frac{1}{\Delta}\widehat{C_*^n k_{sgs}^{\frac{3}{2}}}\right)\frac{\widehat{\Delta}}{K^{3/2}}. \qquad (8)$$

The idea is to include all local dynamic information through the source terms of the transport equation for k_{sgs}. This is probably physically more sound since large local variations in C appear only in the source term, and the effect of the large fluctuations in the dynamic coefficients will be smoothed out in a natural way. In this way, it turns out that the need to restrict or limit the dynamic coefficient is eliminated altogether.

Results

Channel Flow

The flow in a plane channel was computed for $Re_\tau = 395$. A mesh with $64 \times 64 \times 64$ cells was used, with $x_{max} = 2\pi$, $y_{max} = 2$ and $z_{max} = \pi$. The grid is refined near the walls using geometric stretching with an expansion factor of 1.08. The node adjacent to the walls is located at $y/h = 0.003725$, which gives $y^+ = 1.47$. The time step was set to $\Delta t = 0.0012$, which corresponds to a maximum convective CFL of approximately 0.4. Sampling was performed during the last 3000 time steps. All results were averaged in time as well in the streamwise (x) and spanwise (z) directions. The model presented above [3] (Model D) was used.

The mean velocity and normal stresses $\langle u_i^2\rangle_{xzt} = \langle \bar{u}_i^2\rangle_{xzt} - \langle \bar{u}_i\rangle_{xzt}^2$ are compared with DNS data Kim [14] in Fig. 1a,b. The agreement is, as can be seen, fairly good.

The dynamic coefficients are presented in Fig. 1c, and C is found to be approximately 0.03 and C_* close to 0.4. Kim & Menon [15] apply their dynamic one-equation model to plane Couette flow. Their value for C is similar to that in the present work, but their C_* is approximately 3 times larger. The time-averaged value of the homogeneous coefficient is $\langle C\rangle_{xyzt} \simeq 0.02$.

The production, $P_{k_{sgs}}$, is shown in Fig. 1d. It has been split into one positive part and negative part according to [27]

$$\begin{aligned}
P^+ &= \frac{1}{2}\langle\left(P_{k_{sgs}} + |P_{k_{sgs}}|\right)\rangle_{xzt} \\
P^- &= \frac{1}{2}\langle\left(P_{k_{sgs}} - |P_{k_{sgs}}|\right)\rangle_{xzt}.
\end{aligned}$$

It can be seen that there is a portion of the production which is negative (backscatter), which reduces the total production, and thereby also k_{sgs} and ν_{sgs}. Recall that in the Germano model only very small magnitudes of negative ν_{sgs} are permitted, but that the magnitude of negative ν_{sgs} is not limited in any way in the present model.

Square Cylinder

The subject of flow past bluff bodies, such as square cylinders, is of relevance to technical problems associated with energy conservation, structural design and acoustic emissions. In recent years, researchers' attention has turned to the use of LES for studying turbulent flow around bluff bodies. Also recently, this flow case was studied experimentally by Lyn and Rodi [20] and Lyn *et al.* [19, 20].

The flow, with $Re \equiv U_\infty d/\nu = 22\,000$, is described in a Cartesian coordinate system (x, y, z) in which the x-axis is aligned with inlet flow direction, the z-axis is parallel with the cylinder axis and the y-axis is perpendicular to both directions. The origin is located at the center of the cylinder. All quantities are made dimensionless by scaling with the side of the cylinder, d, and free-stream velocity, U_∞. Two calculations are carried out for the resolution of $185 \times 105 \times 25$ (Case I) and $265 \times 161 \times 25$ (Case II) grid points in the (x, y, z) directions.

The transient period before the fully developed state is achieved is about 50 time units, which is greater than 6 shedding periods. The number of iterations per time step is about 2. The time-averaged quantities are sampled over about 20 shedding cycles. The model presented above [3] (Model D) was used.

Figs. 2 and 3 compare the time- and spanwise-averaged resolved-velocity and Reynolds stresses along the centerline of the wake and along the y direction at the position of two diameters downstream of the body with experimental results [19, 20]. The streamwise velocity, $\bar{u}$, at the centerline of the wake is shown in Fig. 2. The minimum streamwise velocity and the extent of the recirculation region of the present study are lower than the experimental values. The recovery of the streamwise velocity levels off at approximately 0.75 and 0.7 for Cases I and II, respectively, which is higher than the experiments, which is

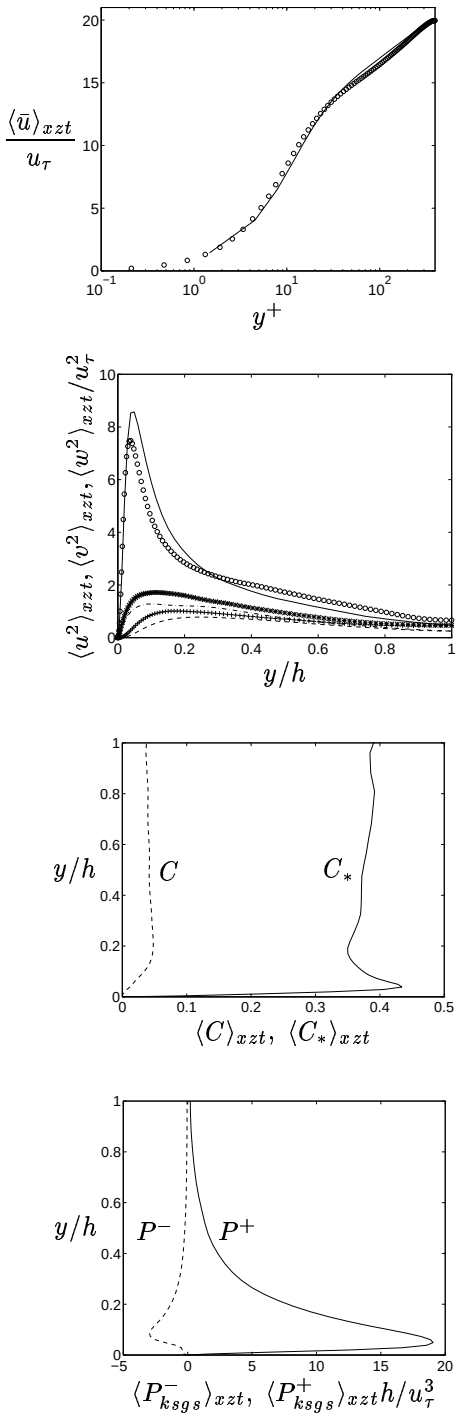

Figure 1: Channel flow. Model D. $Re_\tau = 395$. Markers: DNS [14].

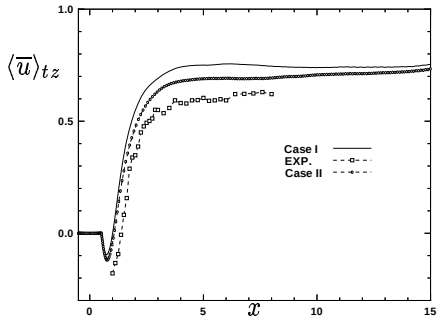

Figure 2: Time- and spanwise-averaged velocity, $\langle\overline{u}\rangle_{tz}$, at centerline ($y = 0$).

at about 0.6. Of these two cases, the finer resolution (Case II) has the larger recirculation length, l_r, larger negative streamwise velocity in the recirculation region and lower recovery of the streamwise velocity the along centerline, which show better agreement with experiments. This finding shows that a part of difference between experiment and numerical simulations for the recovery of the centerline velocity and l_r, which was also noted in Refs. [28, 32], is caused by poor resolution.

Figure 4 presents the time history of the local dynamic coefficient C (see Eq. 6) and the homogeneous coefficient (see Eq. 7). The local coefficient is shown for two grid nodes, one in the stagnation region upstream of the cylinder and one in the wake. Recall that a negative C corresponds to negative production, i.e. backscatter. It can be seen that, at the grid node in the stagnation region, C is always negative. In this region, the irrotational strains, $\partial\bar{u}/\partial x, \partial\bar{v}/\partial y$, are much larger than the rotational strains, $\partial\bar{u}/\partial y, \partial\bar{v}/\partial x$. The flow in the stagnation region is decelerating so that $\partial\bar{u}/\partial x \simeq -\partial\bar{v}/\partial y < 0$ ($\partial\bar{w}/\partial z \simeq 0$). The normal dynamic Leonard stresses, $\mathcal{L}_{11}, \mathcal{L}_{22}$ in Eq. 6, are always positive, and it is found that $\mathcal{L}_{22} > \mathcal{L}_{11}$. Thus $\mathcal{L}_{22}M_{22} + \mathcal{L}_{11}M_{11} > 0$ in Eq. 6, which is why $C < 0$. Figure 4b shows the time history of the homogeneous coefficient, $\langle C\rangle_{xyz}$. As can be seen, the frequency of the homogeneous coefficient is much lower than the local one. The time-averaged value is $\langle C\rangle_{xyzt} \simeq 0.085$

For greater detail, see Sohankar [29, 30].

Surface-Mounted Cube

The surface-mounted cubical obstacle is placed on a channel wall at $Re = 40\,000$ based on the incoming mean bulk velocity and the obstacle height. Two different dynamic subgrid models are used: the model presented above [3] (Model D) and the one-equation model by Kim & Menon [15] (Model KM). In Fig. 5, predicted mean velocities and resolved shear stresses are presented along a vertical line above the cube at $x = 0.5$ (x and y denote the streamwise and normal directions, respectively); the cube is located between $x = 0$ and $x = 1$. As can be seen, the predictions without any model give poor agreement, whereas the two subgrid models give good agreement with experiments. The separation region without any model is much too thin. This is probably because, without a model, the resolved fluctuations are not damped by any subgrid viscosity, and the resolved fluctuations consequently become too large. This gives too a large turbulent diffusion, thus making the separation region become smaller and thinner. It can be seen in Fig. 5b that the resolved shear stress $\langle uv\rangle_t$ without a model is not larger than those obtained with a model;

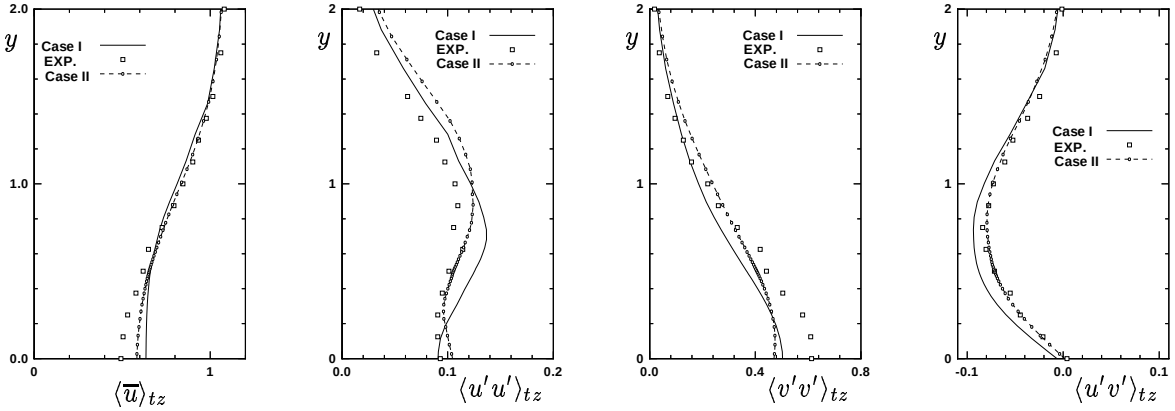

Figure 3: Mean velocity, $\langle\overline{u}\rangle_{tz}$, and turbulent stresses ($\langle u'u'\rangle_{tz}$, $\langle v'v'\rangle_{tz}$, $\langle u'v'\rangle_{tz}$) versus y at $x = 2.5$.

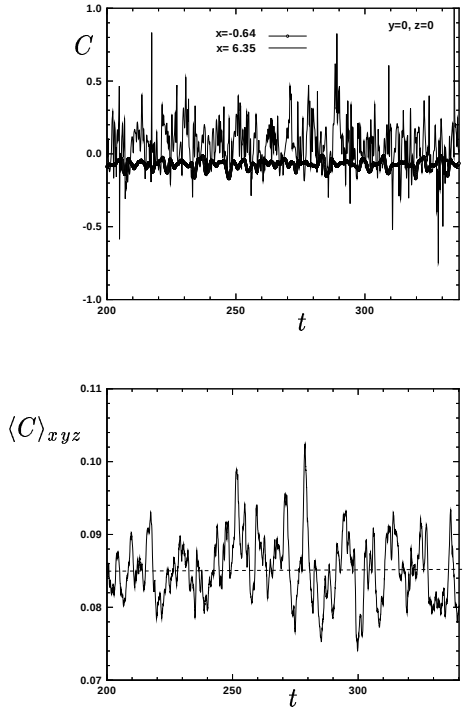

Figure 4: Top: Time history of the C at two chosen cells on the centerline; bottom: Time history of the $\langle C\rangle_{xyz}$.

however, care should be taken when comparing these, since the time-averaged velocity fields are very different. Instead, we could argue as follows: the resolved shear stress without any model is of the same magnitude as with a model, although the velocity gradient of the time-averaged velocity field without any model is much smaller; thus, taking into account the difference in the time velocity fields, the resolved shear stress without a model is indeed larger.

The time history of the dynamic coefficient, C, and the dissipation coefficient, C_*, are shown for the two subgrid models in Fig. 6. It can be seen that the time history of C is much smoother for model KM than for Model D. In Model D, similarity assumptions are made between the grid level (length scale $\ell < \Delta$, velocity scale $k_{sgs}^{\frac{1}{2}}$) and the test level (length scale $\ell < \widehat{\Delta}$, velocity scale $K^{\frac{1}{2}}$). However, in Model KM, the similarity assumption is made between the grid level and the intermediate level (length scale $\Delta < \ell < \widehat{\Delta}$, velocity scale $[0.5\mathcal{L}_{kk}]^{\frac{1}{2}}$), i.e.

$$\begin{aligned} \tau_{ij}^a &= -2C\Delta k_{sgs}^{\frac{1}{2}}\bar{S}_{ij}, \quad \mathcal{L}_{ij}^a = -2C\widehat{\Delta}\,(0.5\mathcal{L}_{kk})^{\frac{1}{2}}\,\widehat{\bar{S}}_{ij} \\ \Rightarrow C &= \frac{1}{2}\frac{\mathcal{L}_{ij}\sigma_{ij}}{\sigma_{ij}\sigma_{ij}}, \quad \sigma_{ij} = -\widehat{\Delta}\,(0.5\mathcal{L}_{kk})^{\frac{1}{2}}\,\widehat{\bar{S}}_{ij}. \end{aligned}$$

The denominator, $\sigma_{ij}\sigma_{ij}$, does not tend to zero as much as the denominator, $M_{ij}M_{ij}$, in Model D, which explains why C does not oscillate as much in Model KM. The time history of coefficient C_* in front of the dissipation term (see Eq. 8) is also smoother in Model KM than in Model D, although the difference is much smaller than for C. The dissipation coefficient often tends to zero (it is restricted so that $C_* \geq 0$) but never becomes larger than 5. Both one-equation models are able to predict negative production (backscatter). The strongest backscatter occurs near the front vertical corners. The magnitude of negative production is higher for Model D than for Model KM. In Model KM, the local coefficient is used in the momentum equation (with the restriction $\nu + \nu_{sgs} \geq 0$), which makes the model less stable. No stability problems were encountered for the surface-mounted cube, but when Model KM and Model D were used to compute the flow in an enclosed cavity [22], stability problems were encountered with Model KM while Model D did not cause any problems.

For greater detail, see Krajnović [16, 17].

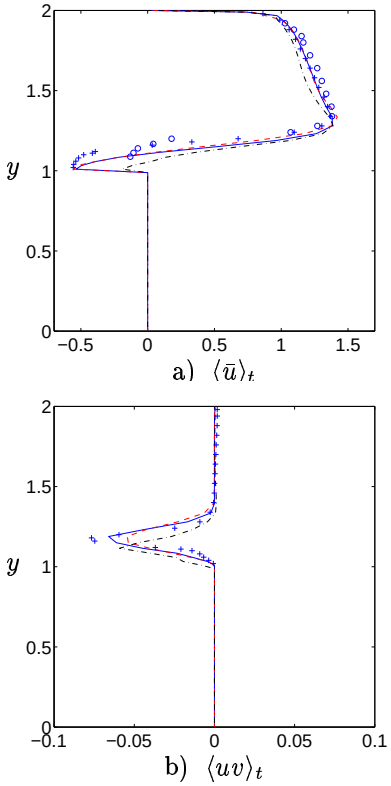

Figure 5: Surface-mounted cube. $z = W/2$ (center plane), $x = 0.5$. Comparison between Model D (dashed line), Model KM (solid line) and calculation without model (dash-dotted line). a) mean velocity $\langle \bar{u} \rangle_t$. b) resolved mean turbulent stresses $\langle uv \rangle_t$.

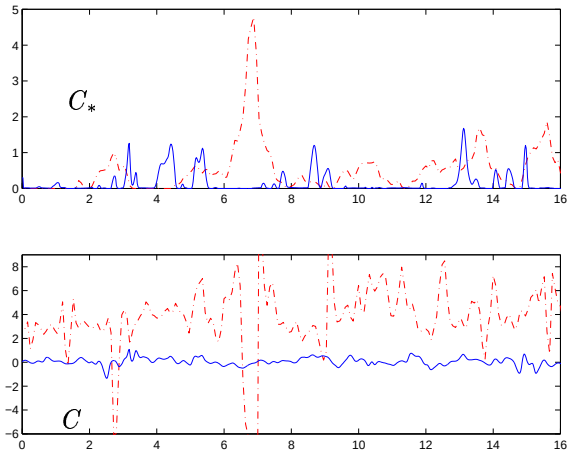

Figure 6: Dynamic coefficients C_* and C. Solid line: Model KM; dash-dotted line: Model D.

Natural Convection

Computation of turbulent natural convection flows represents a challenging aspect of turbulence modeling, where the buoyancy significantly interferes with the turbulence evolution and consequently affects the structure of the mean flow field. In LES for buoyancy-driven flows, the eddy viscosity/diffusivity models have shown rather successful performance, where the Rayleigh-Bénard convection has often been employed for model validation and comparison.

Eidson [7] derived the SGS eddy viscosity with a buoyancy term included in the SGS turbulent production. This gives rise to the *buoyancy model* in which the SGS eddy viscosity takes the form of

$$\nu_{sgs} = C\Delta^2 \left(\mid \bar{S} \mid^2 + \frac{\beta}{Pr_t} \frac{\partial \bar{\theta}}{\partial x_j} g_k \delta_{kj} \right)^{\frac{1}{2}}. \tag{9}$$

In Eq. 9, g_k denotes the gravitational vector, $g_k = (0, -g, 0)$. The $1/\mathcal{T}_B$ scaling that appears in the buoyancy model is then

$$\frac{1}{\mathcal{T}_B} = \left(\mid \bar{S} \mid^2 - \frac{g\beta}{Pr_t} \frac{\partial \theta}{\partial x_j} \delta_{2j} \right)^{\frac{1}{2}}. \tag{10}$$

With this $1/\mathcal{T}_B$ scaling, the sub-grid eddy viscosity must be constrained to be equal to zero, as $\mid \bar{S} \mid^2 < \frac{g\beta}{Pr_t} \frac{\partial \theta}{\partial x_j} \delta_{2j}$. Winckelmans *et al.* [33] evaluated several base models with different choices for the $1/\mathcal{T}$ scaling in an *a priori* test of SGS models using available DNS data. It was found that the choice of $1/\mathcal{T}$ scaling in the sub-grid eddy viscosity is unimportant as it does not significantly affect the correlations between modelled and exact SGS quantities. This suggests that the $1/\mathcal{T}$ scaling does not necessarily need to be derived from the production-dissipation equilibrium argument. Moreover, the problem of inducing non-real solutions with the buoyancy base model, i.e. Eq. 10, must be eliminated. We thus have proposed the new $1/\mathcal{T}_N$ scaling as [25, 26]

$$\frac{1}{\mathcal{T}_N} \equiv \bar{N} = \frac{1}{\mid \bar{S} \mid} \left(\mid \bar{S} \mid^2 - \frac{g\beta}{Pr_t} \frac{\partial \theta}{\partial x_j} \delta_{2j} \right). \tag{11}$$

This model is denoted Model PD. The model coefficients for sub-grid eddy viscosity C, thermal diffusivity C_t and the subgrid Prandtl number, Pr_t, are dynamically determined. The dynamic coefficients are averaged in the periodic directions.

For greater detail, see Peng [25, 26].

Rayleigh-Bénard Convection

The Rayleigh-Bénard convection is induced in a horizontal channel by a heated bottom boundary and a cooled top boundary. The Rayleigh number and the molecular Prandtl number are $Ra = 3.8 \times 10^5$ and $Pr = 1.0$, respectively. The computational domain used is $6 \times 1 \times 6$, with a grid resolution of $48 \times 48 \times 48$. The boundary condition for the pressure is the Neumann condition at the top and bottom wall surfaces. Periodical boundary conditions were employed for all variables in the longitudinal and spanwise directions ($x-$ and $z-$directions). The no-slip condition is used at the walls for the velocity components, $\bar{u}_i$. Constant temperatures are specified at the horizontal wall surfaces, with a temperature difference of $\Delta\theta = 10^o C$. The computation started with a result computed using the Smagorinsky model. The time unit in the Rayleigh-Bénard convection is $t_0 = D/u_0$, where D is the height of the fluid layer, $u_0 = \sqrt{g\beta\Delta\theta D}$, and β is the volumetric expansion coefficient. The time interval is about $0.05t_0$. The number of time steps used in each calculation is generally 60 000. This corresponds

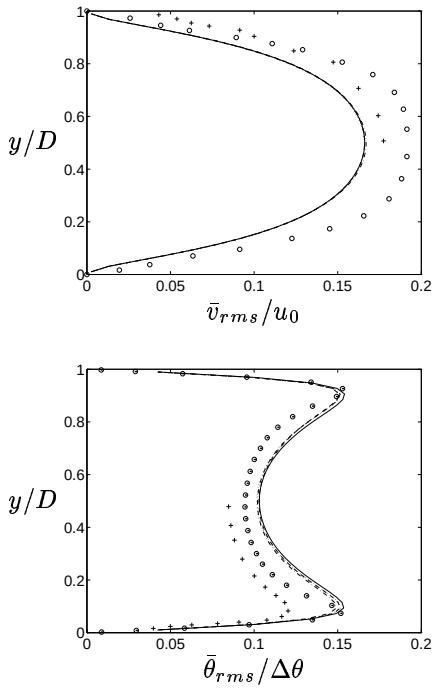

Figure 7: Dotted line: Dynamic model; Dashed line: Model PD ($Pr_t = 0.4$); Solid line: Model PD; Dash-dotted line: Buoyancy model ($Pr_t = 0.4$); + Experimental data from [6]; ∘ DNS data ($Pr = 1.0$) from [21] ⊙ DNS data ($Pr = 0.71$) from [35]

to approximately $3000t_0$. The data are analyzed over a period of about $800t_0$.

The computed vertical distributions for the root mean squares of the vertical velocity component and the temperature $(< (\bar{v} - < \bar{v} >_{xzt})^2 >_{xzt})^{0.5}$ and $(< (\bar{\theta} - < \bar{\theta} >_{xzt})^2 >_{xzt})^{0.5}$, i.e. $\bar{v}_{rms}$ and $\bar{\theta}_{rms}$, are shown in Fig. 7. Model PD produces very similar simulations regardless of whether Pr_t is set as a constant ($Pr_t = 0.4$) or is locally determined except in the near-wall region, where using $Pr_t = 0.4$ gives slightly better distributions. All the models give similar and reasonable results in comparison with both the DNS data from [21, 35] and the laboratory data [6]. The $\bar{w}_{rms}$ profile (not shown here) is nearly identical to the $\bar{u}_{rms}$ profile. In Fig. 7, the experimental data are adopted from Deardorff and Willis' laboratory investigation [6] for $Ra = 6.3 \times 10^5$. All the models under-predict $\bar{v}_{rms}$ in the core region of the flow domain as compared with the measured and DNS data, but give better predictions than those in [34] for the same flow problem, where the buoyancy model (termed *stratification formulation* in [34]) was applied. The comparison with the experimental data shows that the $\bar{\theta}_{rms}$ profile is generally over-predicted by all the models. Eidson [7] showed a similar prediction in a previous LES. The results, however, agree better with the DNS data for $Pr = 0.71$ given by Wörner and Grötzbach [35]. In the DNS by Moeng and Rotunno [21], with $Pr = 1.0$, it was stated that the root-mean-square of the temperature has a maxima of 0.15 located about 0.07 from both walls and a value of about 0.08 at mid-level. This has been approximately reflected in the present prediction, as shown in Fig. 7.

For greater detail, see Peng [25, 26].

Infinite Cavity

As to the flow arising between two differentially heated, infinite vertical walls, this is statistically of a one-dimensional type along the vertical/streamwise direction with no thermal stratification.

The computation was made for an air-filled configuration with dimensions of $W \times H \times L = 0.1 \times 0.25 \times 0.1$ in the $x-$, $y-$ and $z-$directions, respectively. The Rayleigh number based on the gap width between the side walls, W, i.e. $Ra = g\beta\Delta\theta W^3/\nu\alpha$, is 5.4×10^5. The temperature difference between the two isothermal walls is $\Delta\theta = \theta_h - \theta_c = 5.3^oC$. Non-uniform grid is employed only in the $x-$direction, with $64 \times 64 \times 32$ meshes to discretize the computational domain. A periodic condition has been used for homogeneous boundaries in the $y-$ and $z-$directions.

The time step adopted in the computation is about $\Delta t = 23.3W/V_b$. The time period used for averaging in data analyses is about $100000\Delta t$.

The computed profiles for the mean streamwise velocity given by Model PD are in rather good agreement with the DNS data, while the dynamic model and the Smagorinsky model slightly over-predict the velocities in the outer part of the boundary layer, see Fig. 8. The dynamic models, however, produce results for the vertical heat flux, $< v'\theta' >$, that are in rather good agreement with the DNS data (see Fig. 8), particularly Model PD. The Smagorinsky model, by contrast, over-predicts this quantity by about 20% in the core of the channel and for the near-wall peak.

For greater detail, see Peng [25, 26].

Flow in Rotating Channels

The object of this project [24] is to use LES to study the internal cooling of rotating blades in gas turbines. We are initially studying the flow in a rotating plane channel and a rotating square duct. Periodic boundary conditions are used in the streamwise direction and for the plane channel, also in the spanwise direction. A $66 \times 66 \times 66$-node mesh is used for both configurations. The subgrid model of Kim & Menon [15] is used. Figure 9 compares the streamwise mean velocity component with DNS and shows good agreement.

The flow in a non-rotating, straight duct is symmetric with respect to the corner bisectors, and the secondary flow is driven by the turbulent stresses. The secondary flow is fairly weak with $(|V|)_{max}/U_c = 1.43\%$ [9]. This symmetry is destroyed as rotation is introduced, as the flow is affected by rotation (the Coriolis forces). The secondary flow in Fig. 10 is driven both by turbulent stresses, as in the non-rotating case, as well as by the Coriolis forces. The secondary flow is much stronger, and our preliminary results show that $(|V|)_{max}/U_c = 2.6\%$.

LESFOIL

LESFOIL is a Brite-Euram project coordinated by the author. The project is focused on LES around airfoils. Active in the project are four universities, two research institutes, and three industrial partners (see http://www.tfd.chalmers.se/~lada/projects/lesfoil/proright.html).

Given the starting position of the partners, the existing experience and knowledge of LES, it is expected that very rapid progress can be achieved on the performance of an initial LES of flow around a simple airfoil. A considerable part of the supported time will be spent in carefully analyzing results of such a simulation in order to optimize the numerical methods, investigate the size and refinement of the mesh required for a useful LES to be carried out for airfoils, near-wall treatment, and investigate alternative subgrid models. Since traditional RANS performs rather well for attached flow around airfoils, we are direct-

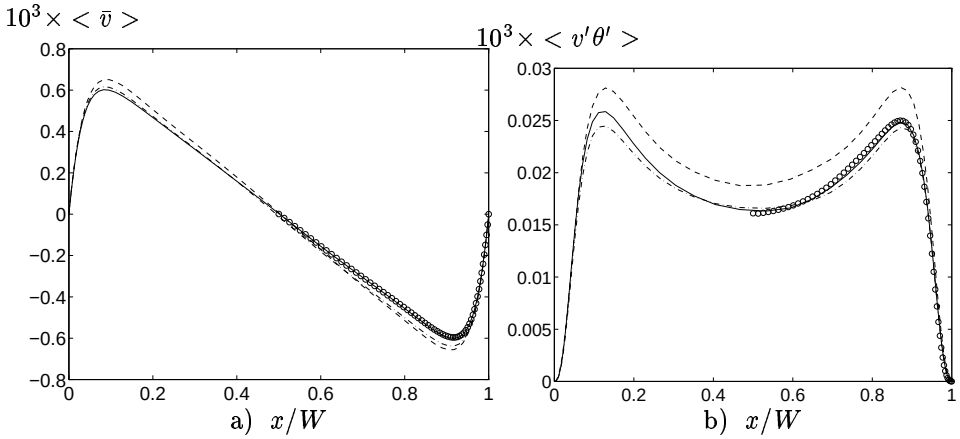

Figure 8: Dashed line: the Smagorinsky model; Dash-dotted line: the dynamic Smagorinsky model; Solid line: Model PD; ○: DNS data.

ing our efforts toward high-lift airfoils. The A-profile ($Re = 2.1 \cdot 10^6$, $Ma = 0.15$) will be the main test case.

The objectives of the project are:

- To provide know-how on an advanced CFD method to the European aeronautical industry;
- To determine the feasibility of LES for the European aeronautical industry;
- To demonstrate the feasibility of LES for flow over an airfoil;
- To assess the computational requirements for carrying out LES for the simple airfoil and for more complex configurations in the future;
- To develop highly efficient numerical methods for the LES of airfoil flows;
- Comparisons of competing (dynamic) subgrid-scale models for these flows.

The work is divided into three Tasks.

- Development of subgrid models. If reliable subgrid models are developed, a larger portion of the turbulence could be modelled, allowing coarser grids.
- Development of efficient numerical parallel methods. LES is computationally very expensive, and thus it is extremely important to reduce the computation time as much as possible.
- Near-wall treatment. At high Reynolds numbers, LES requires a fine grid in all three coordinate directions. The use of wall functions or simple RANS (Reynolds Averaging Navier-Stokes) turbulence models in the near-wall region will be studied. This would allow us to use coarser grid spacing, especially in the streamwise and spanwise directions.

Future Work

To perform LES at high Re numbers seems to require extremely fine grids. Compared to RANS the grid needs to be fine especially in the streamwise and spanwise directions. An interesting approach was proposed by Spalart *et al.* [31], where they combine LES and RANS, using a one-equation subgrid/turbulence model. In this way RANS could be used in attached boundary layers, and LES could be used in shear layers and wakes to resolve large, turbulent scales. The main advantage of this approach is that coarser grid – in the streamwise and spanwise directions – can be used in the attached boundary layers, which would reduce the required CPU time considerably.

References

[1] S. Dahlström and L. Davidson. Chalmers' contribution to the 6-months report, lesfoil: A brite-euram project. Technical report, Dept. of Thermo and Fluid Dynamics, Chalmers, 1997.

[2] S. Dahlström and L. Davidson. Chalmers' 12-months report, lesfoil: A brite-euram project. Technical report, Dept. of Thermo and Fluid Dynamics, Chalmers, 1999.

[3] L. Davidson. Large eddy simulation: A dynamic one-equation subgrid model for three-dimensional recirculating flow. In *11th Int. Symp. on Turbulent Shear Flow*, volume 3, pages 26.1–26.6, Grenoble, 1997.

[4] L. Davidson. Large eddy simulations: A note on derivation of the equations for the subgrid turbulent kinetic energies. Rept. 97/11, Dept. of Thermo and Fluid Dynamics, Chalmers, 1997.

[5] L. Davidson. LES of recirculating flow without any homogeneous direction: A dynamic one-equation subgrid model. In K. Hanjalić and T.W.J. Peeters, editors, *2nd Int. Symp. on Turbulence Heat and Mass Transfer*, pages 481–490, Delft, 1997. Delft University Press.

[6] J.W. Deardorff and G.E. Willis. Investigation of turbulent thermal convection between horizontal plates,. *Journal of Fluid Mechanics*, 28:675–704, 1967.

[7] T.M. Eidson. Numerical simulation of the turbulent Rayleigh-Bénard problem using subgrid modelling. *Journal of Fluid Mechanics*, 158:245–268, 1985.

[8] P. Emvin. *The Full Multigrid Method Applied to Turbulent Flow in Ventilated Enclosures Using Structured and Unstructured Grids.* PhD thesis, Dept. of Thermo and Fluid Dynamics, Chalmers, 1997.

[9] S. Gavrilakis. Numerical simulations of low-Reynolds-number turbulent flow through a straight square duct. *Journal of Fluid Mechanics*, 244:101–129, 1992.

[10] M. Germano, U. Piomelli, P. Moin, and W.H. Cabot. A dynamic subgrid-scale eddy viscosity model. *Physics of Fluids A*, 3:1760–1765, 1991.

[11] M. Germano, U. Piomelli, P. Moin, and W.H. Cabot. Erratum. *Physics of Fluids A*, 3:3128, 1991.

[12] S. Ghosal, T.S. Lund, P. Moin, and K. Akselvoll. Corrigendum. *Journal of Fluid Mechanics*, 297:402, 1995.

[13] S. Ghosal, T.S. Lund, P. Moin, and K. Akselvoll. A dynamic localization model for large-eddy simulation of turbulent flows. *Journal of Fluid Mechanics*, 286:229–255, 1995.

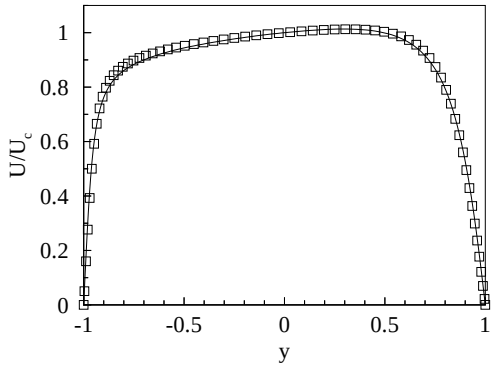

Figure 9: Mean streamwise velocity in the rotating channel. $Re_\tau = 194$. Line: DNS [18]. ($Ro_\tau = 1.56$). Symbols: Present results ($Ro_\tau = 1.50$, $Ro = 0.1$.).

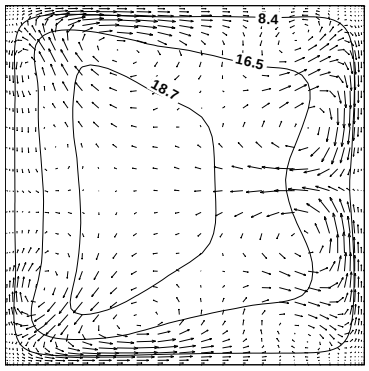

Figure 10: Mean flow in a rotating, square duct. $Re_\tau = 300$, $Ro_\tau = 0.15$ ($Ro = 0.01$). The velocity vectors show the secondary flow. Iso-contours of $\langle \bar{u} \rangle_{xt}/u_\tau$.

[14] J. Kim. The collaborative testing of turbulence models (organized by P. Bradshaw *et al.*). Data Disk No. 4 (also available at Ercoftac's www-server `http://fluindigo.mech.surrey.ac.uk/database`), 1990.

[15] W.-W. Kim and S. Menon. Application of the localized dynamic subgrid-scale model to turbulent wall-bounded flows. AIAA 97-0356, Reno, 1997.

[16] S. Krajnović. Large-eddy simulation of the flow around a surface-mounted single cube in a channel. Rept. 98/7, Dept. of Thermo and Fluid Dynamics, Chalmers, 1998.

[17] S. Krajnović and L. Davidson. Large-eddy simulation of the flow around a surface-mounted cube using a dynamic one-equation subgrid model (to be presented). In *The First International Symp. on Turbulence and Shear Flow Phenomena, Santa Barbara, Sept. 12-15*, 1999.

[18] R. Kristoffersen and H.I. Andersson. Direct simulations of low-Reynolds-number turbulent flow in a rotating channel. *Journal of Fluid Mechanics*, 256:163–197, 1993.

[19] D.A. Lyn, S. Einav, W. Rodi, and J.-H. Park. A laser-doppler velocimetry study of ensemble-averaged characteristics of the turbulent near wake of a square cylinder. *Journal of Fluid Mechanics*, 304:285–319, 1995.

[20] D.A. Lyn and W. Rodi. The flappying shear layer formed by flow separation from the forward corner of a square cylinder. *Journal of Fluid Mechanics*, 267:353–376, 1994.

[21] C.-H. Moeng and R. Rotunno. Vertical-velocity skewness in the buoyancy-driven boundary layer. *J. Atmos. Sci.*, 47:1149–1162, 1990.

[22] D. Müller and L. Davidson. private communication. Dept. of Thermo and Fluid Dynamics, Chalmers, 1998.

[23] H. Nilsson and L. Davidson. CALC-PVM: A parallel multiblock SIMPLE multiblock solver for turbulent flow in complex domains. Rept. 98/12, Dept. of Thermo and Fluid Dynamics, Chalmers, 1998.

[24] J. Pallares and L. Davidson. private communication. Dept. of Thermo and Fluid Dynamics, Chalmers, 1998.

[25] S.-H. Peng. *Modeling of Turbulent flow and Heat Transfer Modelling for Building Ventilation.* PhD thesis, Dept. of Thermo and Fluid Dynamics, Chalmers, 1998.

[26] S.-H. Peng and L. Davidson. Comparison of subgrid-scale models in LES for turbulent convection flow with heat transfer. In *2nd EF Conference in Turbulent Heat Transfer*, volume 1, pages 5.24–5.35, Manchester, 1998.

[27] U. Piomelli, W.H. Cabot, P. Moin, and S. Lee. Subgrid-scale backscatter in turbulebt and transitional flows. *Physics of Fluids A*, 3:1766–1771, 1991.

[28] W. Rodi, J.H. Ferziger, M. Breuer, and M. Pourquié. Status of large-eddy simulations: Results of a workshop. *J. Fluids Engineering*, pages 248–262, 1997.

[29] A. Sohankar. *Numerical Investigation of Vortex Shedding Around Square Cylinders at Low Reynolds NUmber.* PhD thesis, Dept. of Thermo and Fluid Dynamics, Chalmers, 1998.

[30] A. Sohankar, L. Davidson, and C. Norberg. A dynamic one-equation model for simulation of flow around a square cylinder (to be presented). In *4th International Symposium on Engineering Turbulence Modelling and Measurements, Corsica, May 24-26*, 1999.

[31] P.R. Spalart, W.-H. Jou, M.Strelets, and S.R. Allmaras. Comments on the feasability of LES for wings and on a hybrid RANS/LES approach. In C. Liu and Z. Liu, editors, *Advances in LES/DNS, First Int. conf. on DNS/LES*, Louisiana Tech University, 1997. Greyden Press.

[32] P. R. Voke. Flow past a square cylinder: Test case LES2. In J. P. Chollet et al., editor, *Direct and Large Eddy Simulation II.* Kluwer Academic Publishers, 1997.

[33] G.S. Winckelmans, T.S. Lund, D. Carati, and A.A. Wray. A priori testing of subgrid-scale models for the velocity-pressure and vorticity-velocity formulations. In *Proc. Summer Program*, pages 309–328, Center for Turbulent Research, Stanford Univ./NASA Ames Reseach Center, 1996.

[34] V.C. Wong and D.K. Lilly. A comparison of two dynamic subgrid closures methods for turbulent thermal convection. *Physics of Fluids A*, 6:1016–1023, 1994.

[35] M. Wörner and G. Grötzbach. DNS database of turbulent convection in horizontal fluid layers. http://hbksun17.fzk.de:8080/IRS/eng/IRS3/TURBIT_DNS_database.html, 1996.

[36] I. Zacharov. private communication. European Supercomputer Team, Silicon Graphics Inc., Switzerland, 1997.